

Fadlallah

Structural deformation of sandwich composite heliostats

Sulaiman Fadlallah¹, Timothy Anderson¹ and Roy Nates¹

¹*Department of Mechanical Engineering, Auckland University of Technology, Auckland, New Zealand*

E-mail: timothy.anderson@aut.ac.nz

Abstract

The cost of heliostats has a significant influence on the cost of central tower concentrating solar power systems. To address this issue there is a need for innovative heliostat designs that can reduce the heliostats' cost without affecting its tracking performance. One way of reducing this cost is by utilizing lightweight sandwich composites in the design of the heliostat structure. However, there are some challenges in implementing such systems, particularly with respect to wind loads. In this respect, the aim of this study was to computationally investigate the interaction between the wind and sandwich composites employed as a heliostat mirror support structure.

The results show that the maximum resultant displacement of the composite structure heliostat surface was within the commonly accepted limits for optical alignment. This demonstrates the potential for sandwich composites to be utilized in a lightweight heliostat support structure capable of withstanding wind loads.

1. Introduction

Central tower concentrating solar power (CSP) systems offer a promising option for electricity generation. Although central tower CSP systems offer a means of generating high temperatures achieving these high temperatures requires a large number of heliostats. Due to this large number of reflectors, heliostats represent the largest cost element of central tower (CSP) systems: almost 50% of the plant's total cost (Kolb et al., 2007). This has encouraged the development of new innovative heliostat designs and solutions, aiming to reduce the heliostats' cost without affecting its tracking performance.

For both large and small-area heliostats, the drive element holds the most influence on the production cost of heliostats (Kolb et al., 2011). Large-area heliostats require a high-torque drive, due in part to the heavy mirror support structure that is generally designed from steel. A promising opportunity arises for reducing the cost of heliostats by reducing the mirror support structure's total weight while maintaining the required strength to withstand the maximum bending and torsional loads during high winds.

One possible solution is to use honeycomb sandwich composites due to their lightweight properties and high flexural stiffness (Heimbs et al., 2008; Ayub et al., 2011). This type of composite is frequently used in automotive, marine and aerospace structures and is formed by adhering two thin-face sheets to a low-density honeycomb core. By design, the honeycomb core is capable of withstanding transverse normal and shear loads (Zenkert, 1997) while the faces handle both compressive and tensile loads due to bending.

Given that honeycomb sandwich composites are widely integrated into many modern structural applications, this work set out to investigate their suitability for use as a heliostat mirror structure.

2. Method

In order to assess the suitability of honeycomb sandwich composites as a heliostat structure, particularly under wind loading, it was decided to perform a fluid structure interaction (FSI) study (combined computational fluid dynamics (CFD) and finite element analysis (FEA)). In doing this, it was assumed that the heliostat would consist of a 148 m² rectangular sandwich composite plate mounted and supported by four steel attachments (Figure 1a). The heliostat's sandwich composite structure (Figure 1b) was assumed to consist of a 300 mm thick aluminum honeycomb core sandwiched between two 0.3 mm aluminum skins with a 4 mm thick glass mirror mounted on top surface of the sandwich composite.

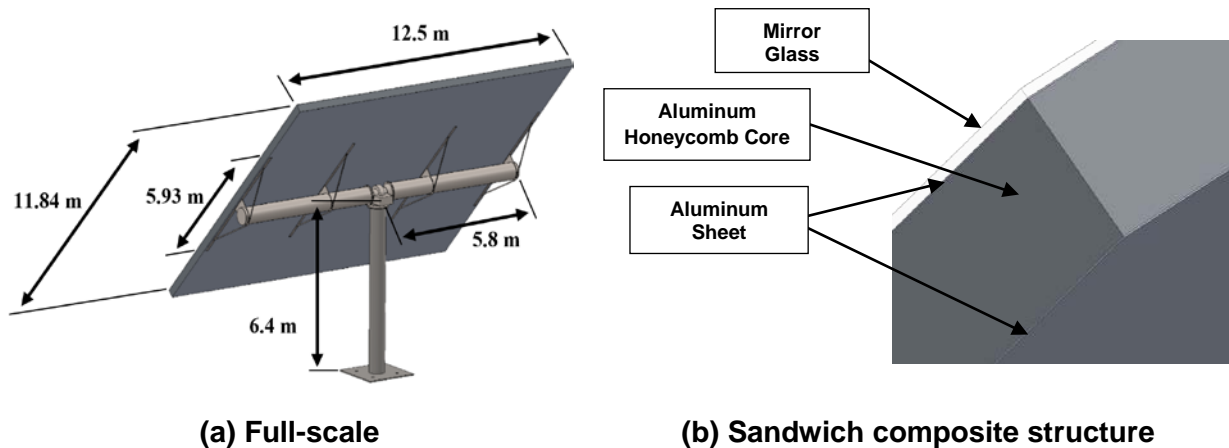


Figure 1. Sandwich composite-based heliostat

In undertaking the analysis, the wind (i.e. the fluid) flow around the heliostat was modelled using ANSYS's commercial CFD software, FLUENT 16.2. Because of its capability of predicting flow separation, the Shear Stress Transport (SST) $k-\omega$ turbulence model was used to resolve the turbulent field for this study (ANSYS, 2015). This model has been effectively employed in atmospheric boundary layer flow simulation in numerous studies (Jubayer and Hangan, 2014; Uzair et al., 2017).

To ensure a sufficiently accurate simulation of the flow, the computational domain around the heliostat (Figure 2) was extended 10L downstream, to capture the wake of the heliostat, 5L upstream to allow the development of a boundary layer on the ground (a description and validation of this approach is provided in Appendix A) and 4L and 6L in the cross-and span-wise directions respectively, where L is the heliostat chord length. The domain was discretised in space with an un-structured mesh, where finer grid elements were employed near the heliostat and in its wake region and the regions away from the heliostat were meshed with larger grid sizes (Figure 3). Mesh sensitivity analysis was performed to investigate the effect of grid sizes on the numerical results. Different grid sizes were tested to check their effects on the drag force coefficient experienced by the heliostat structure (Figure 4). The grid independency test led to a domain consisting of approximately 13 million elements being used. The computational domain's inlet was set as a velocity boundary with wind entering the domain at a velocity of 20 m/s (a Reynolds number of $\sim 1.62 \times 10^7$ taking the chord length of the panel as the characteristic length). The domain's outlet was set as a

zero gauge pressure boundary, and a stationary non-slip wall boundary was used for both the heliostat and the ground. A symmetry boundary was set at the remaining three sides of the computational domain, representing the external flow around the heliostat's structure. The SST k- ω turbulence model constants used in this study are the same as those used by Uzair et al. (2018). Subsequently, CFD simulations were performed to determine the aerodynamic loads on the heliostat for tilt angles (θ) between 90° and -90° as shown in Figure 5.

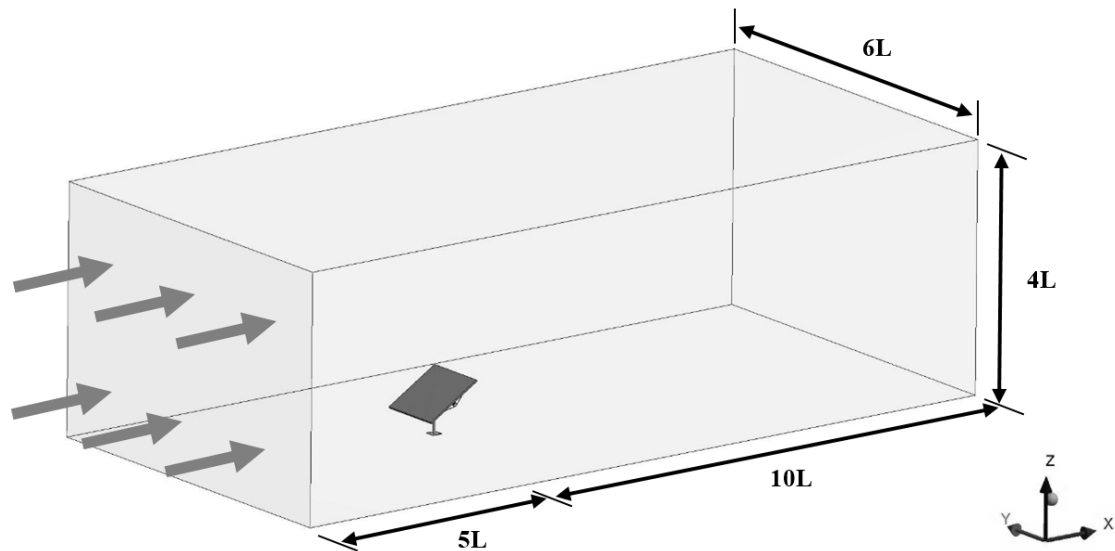


Figure 2. Computational domain

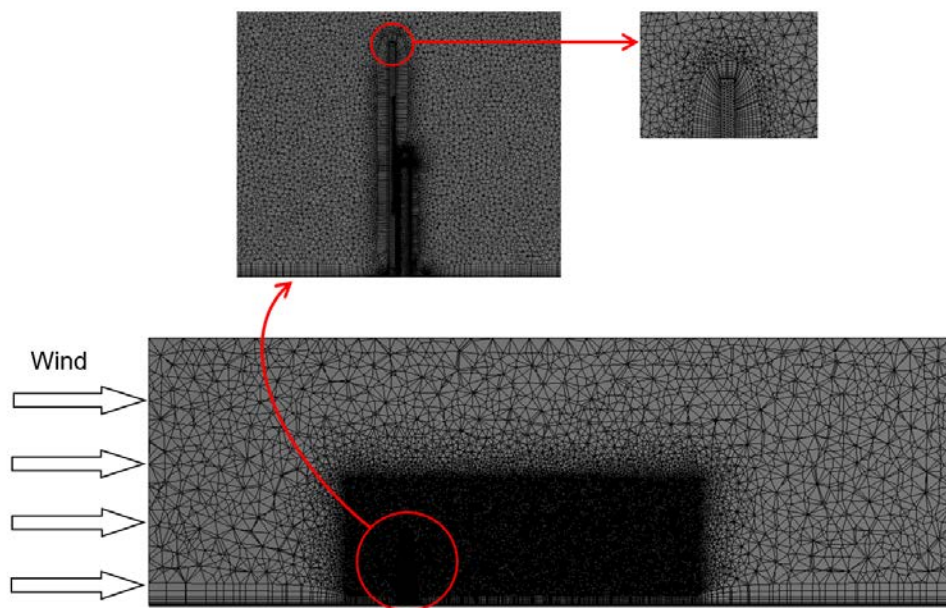


Figure 3. CFD mesh around the heliostat

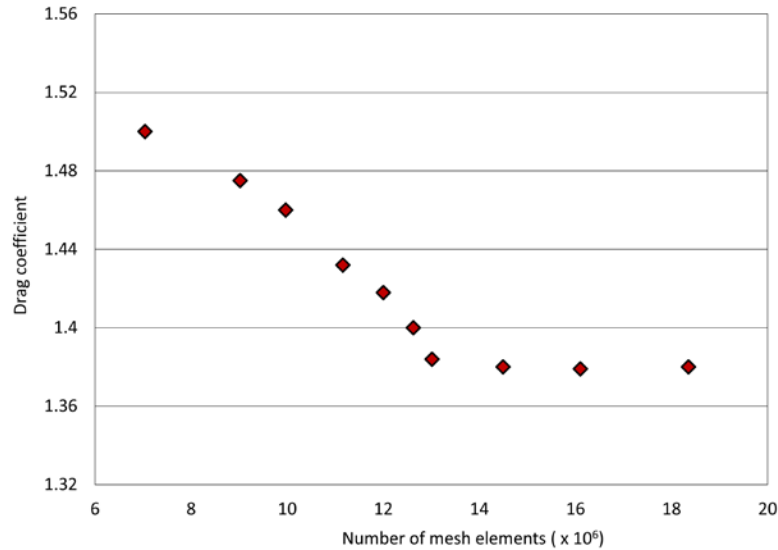


Figure 4. Mesh independency test

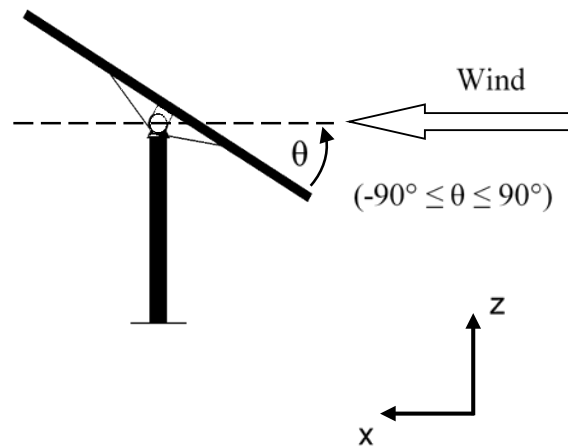


Figure 5. The Coordinate system used in the study

To investigate the behaviour characteristics of the sandwich composite-based heliostat structure under wind loads, the predicted aerodynamic loads were then mapped to an FEA model of the sandwich composite-based heliostat (Figure 6) developed in the ANSYS/Static Structural package. This coupling strategy is a one-way coupling method (as shown in Figure 7), which is less computationally intensive compared than the more complex unsteady two-way approach. In addition, obtaining and verifying the flow characteristics and aerodynamic loads is simpler but more reliable than two-way FSI, where assuring solution convergence and accurate results cannot be guaranteed (Lee et al., 2017). That said, for the FEA fine meshes were generated (about 650,000 elements after performing mesh sensitivity analysis) to reduce any numerical instabilities when importing the aerodynamic loads from the CFD solver.

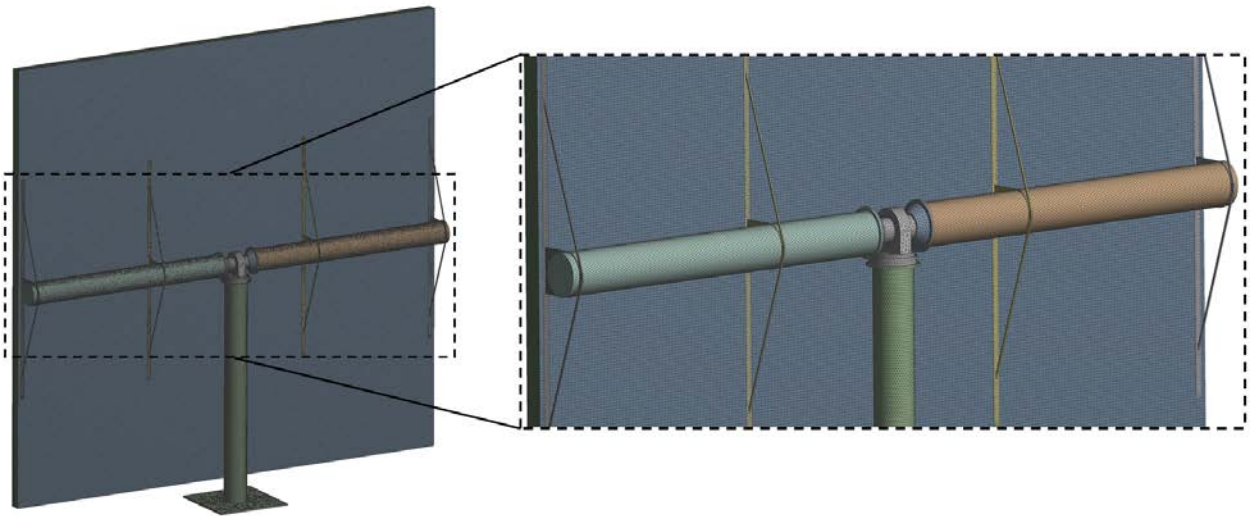


Figure 6. FEA model of the heliostat structure

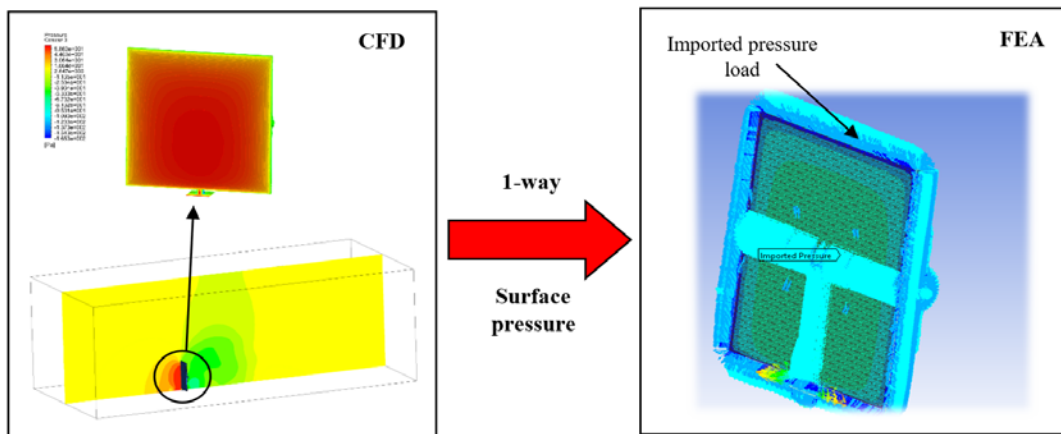
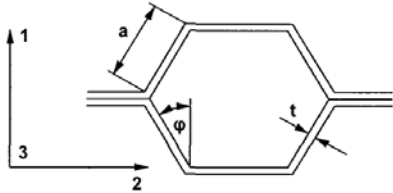


Figure 7. One-way FSI process diagram

Furthermore, rather than developing a fully detailed multi-cell honeycomb core model, the core was modelled using an equivalent three-dimensional orthotropic material model as suggested by Schwingshackl et al. (2006) and Soroohan et al. (2016). In doing this, the honeycomb core's mechanical properties were calculated based on the geometrical properties of the honeycomb shape and the material characteristics using the relationships described by Nast (1997) and Gibson and Ashby (1997) (Appendix B). Table 1 lists the material properties of the aluminum sheets, along with the honeycomb's geometrical properties and the core's calculated properties.

Table 1. Aluminum sheet and aluminum honeycomb core's material properties

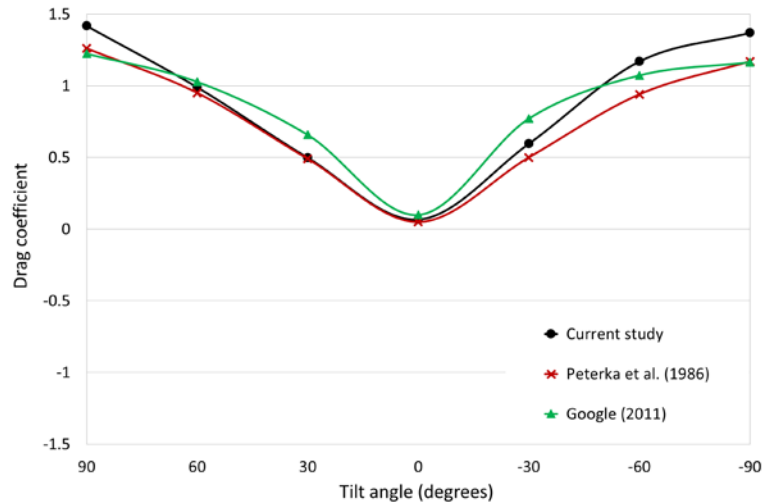
Aluminum Mechanical Properties		
Mechanical Property	Value	Unit
Modulus of elasticity (E)	6.9E10	Pa

	Poisson's ratio (ν)	0.33	-
	Shear modulus (G)	2.7E10	Pa
	Density (ρ)	2700	kg/m ³
Aluminum honeycomb core calculated mechanical properties			
			
Honeycomb cell geometry	Core angle (ϕ)	30	deg
	Cell wall length (a)	6	mm
	Sheet thickness (t)	0.03	mm
Calculated mechanical properties	Modulus of elasticity in direction 1 (E_1)	2.91E04	Pa
	Modulus of elasticity in direction 2 (E_2)	2.23E04	Pa
	Modulus of elasticity in direction 3 (E_3)	5.31E08	Pa
	Poisson's ratio in plane 1-2 (ν_{12})	1.14	-
	Poisson's ratio in plane 2-3 (ν_{23})	1.39E-5	-
	Poisson's ratio in plane 1-3 (ν_{13})	1.81E-5	-
	Shear modulus in plane 1-2 (G_{12})	5.16E03	Pa
	Shear modulus in plane 2-3 (G_{23})	1.54E08	Pa
	Shear modulus in plane 1-3 (G_{13})	2.08E08	Pa
	Density of honeycomb core ($\rho_{\text{honeycomb}}$)	15.59	kg/m ³

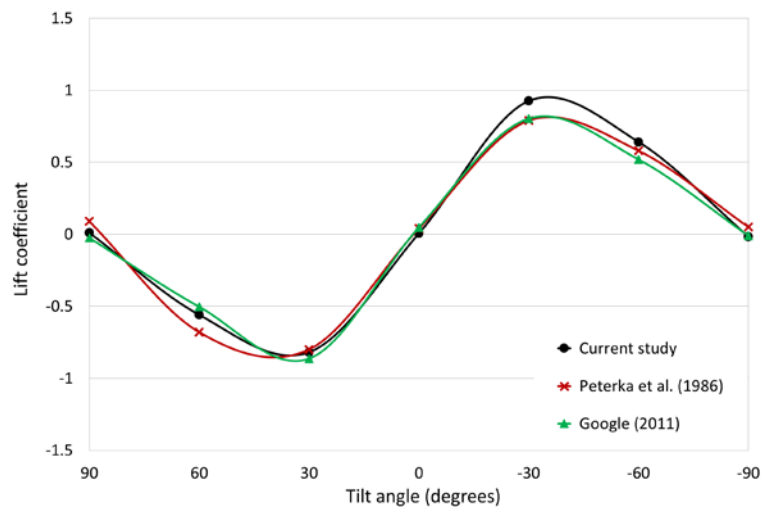
2.1. Validation

Establishing an accurate FSI model for the sandwich composite-based heliostat required obtaining accurate CFD and FEA results. To evaluate the accuracy of the FSI model, both components were validated independently. For the CFD, the heliostat structure's predicted mean drag and lift coefficients for multiple tilt angles were compared with experimental measurements presented by Peterka et al. (1986) and Google (2011) as shown in Figure 8.

Both the drag and lift coefficient predicted values were found to correspond well with those of these previous two studies thus verifying the accuracy of the CFD model.



(a) Drag coefficient



(b) Lift coefficient

Figure 8. Comparison of drag and lift coefficients at different tilt angles

The FEA model, on the other hand, was validated against modal analysis results reported in Gong et al. (2012). Figure 9 shows the sandwich composite-based heliostat's modal frequency results for the case when the structure is tilted at an angle of 90°. It can be seen that the results are in good agreement with literature data, thus demonstrating the validity of the present model.

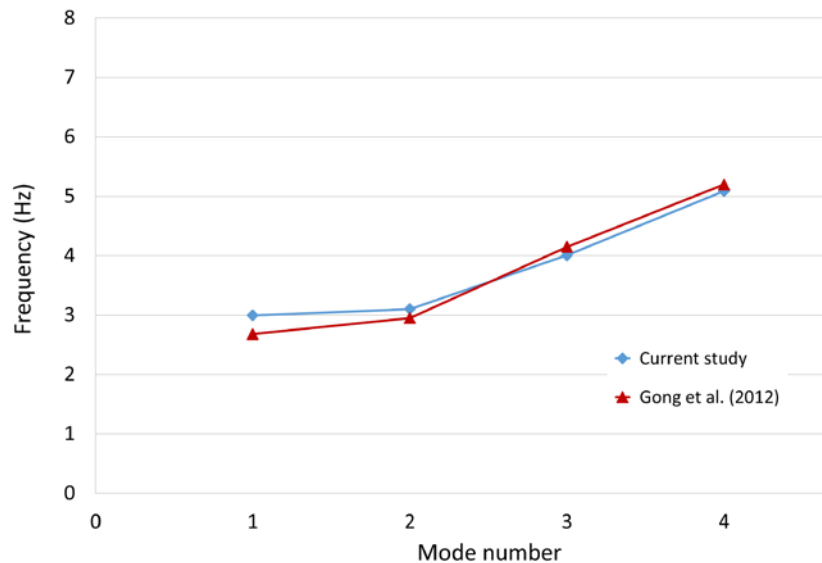


Figure 9. Comparison of mode frequencies of the sandwich composite-based heliostat

3. Results and Discussion

Having demonstrated the validity of the FSI method, Figure 10 shows in detail the wind pressure distributions on the heliostat at a 20 m/s wind speed for a range of tilt angles. For a 90° tilt angle flow is perpendicular to the heliostat's mirror surface which causes the flow's velocity in the front of heliostat structure to move towards a stagnation condition (zero wind velocity). This results in high-pressure values at the middle of a span-wise line and decreases towards the edges. This is expected as the flow accelerates at the edges to maintain continuity and in doing so it creates low-pressure regions on the reflector's surface. Progressively altering the tilt angle from $\theta = 90^\circ$ to $\theta = 30^\circ$ results in a shift in the high pressure region towards the lower edge of the reflector.

Now for stow position (the 0° tilt angle), the wind loading has no noticeable effect on the structure at this configuration compared to the remaining angles of operation. This is due to the fact that the area in the front side of the reflector directly facing the wind is very small, allowing the incoming flow to become uniform and attached to the heliostat's surface. However, what is noticeable from the pressure coefficient distribution on the heliostat at this configurations ($\theta = 0^\circ$) (Figure 11) is that from the windward side the reflector's back surface has greater wind pressures compared to the upper surface. This pressure difference results in large lift forces close to the windward edge. From the leeward side of the heliostat, on the other hand, the opposite occurs and wind pressures are higher at the reflective surface compared to the back surface. This is due to the depression region formed within the torque tube and the reflector's back surface, causing high suction to occur at the heliostat's leeward side.

As the heliostat structure is moved from the stow position to a -90° tilt angle (Figure 10), the incoming wind acts on the back surface of the heliostat directly, resulting in high-pressure values at the middle of the heliostat's back surface.



ASIA-PACIFIC
SOLAR RESEARCH
CONFERENCE

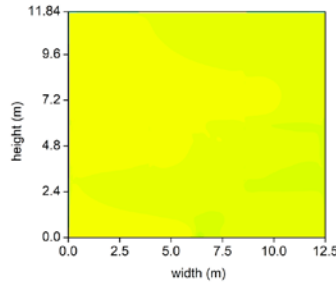
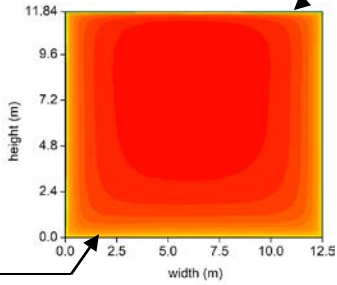
Leeward edge

Windward edge

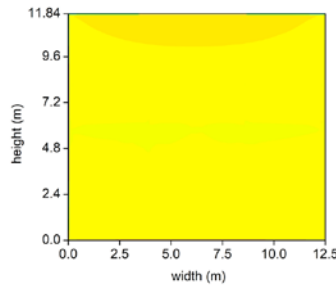
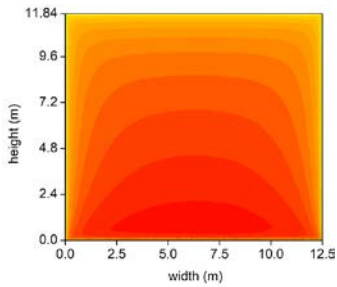
Reflective surface

Back surface

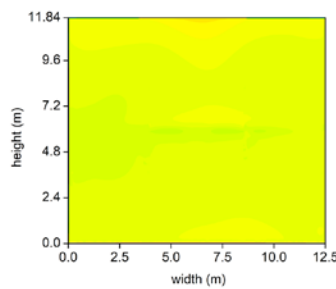
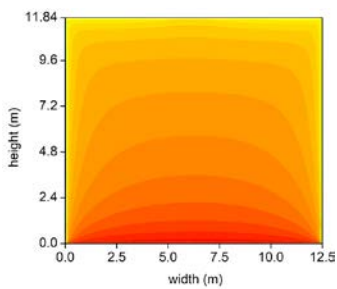
$\theta = 90^\circ$



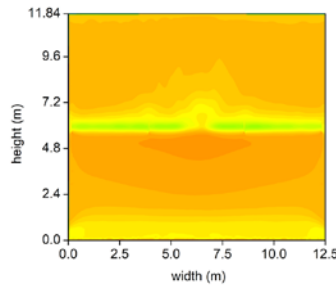
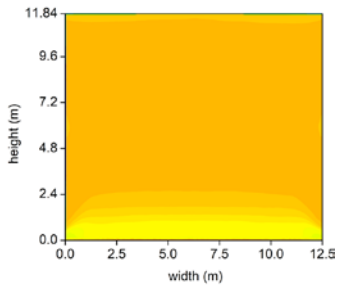
$\theta = 60^\circ$



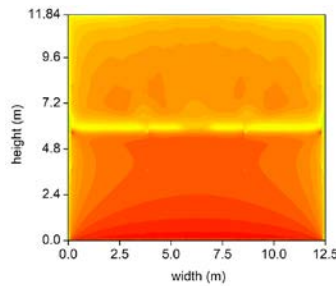
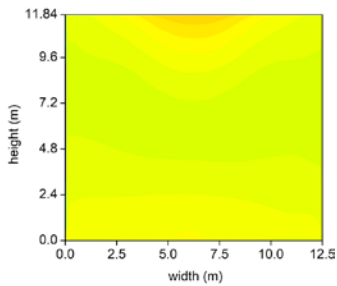
$\theta = 30^\circ$



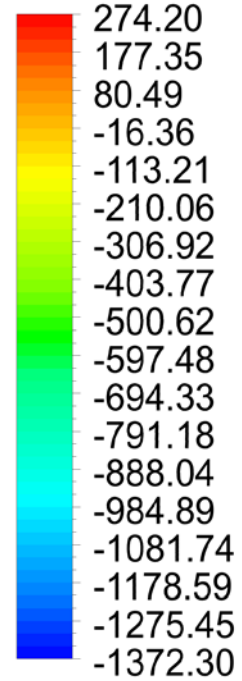
$\theta = 0^\circ$



$\theta = -30^\circ$



Pressure



[Pa]

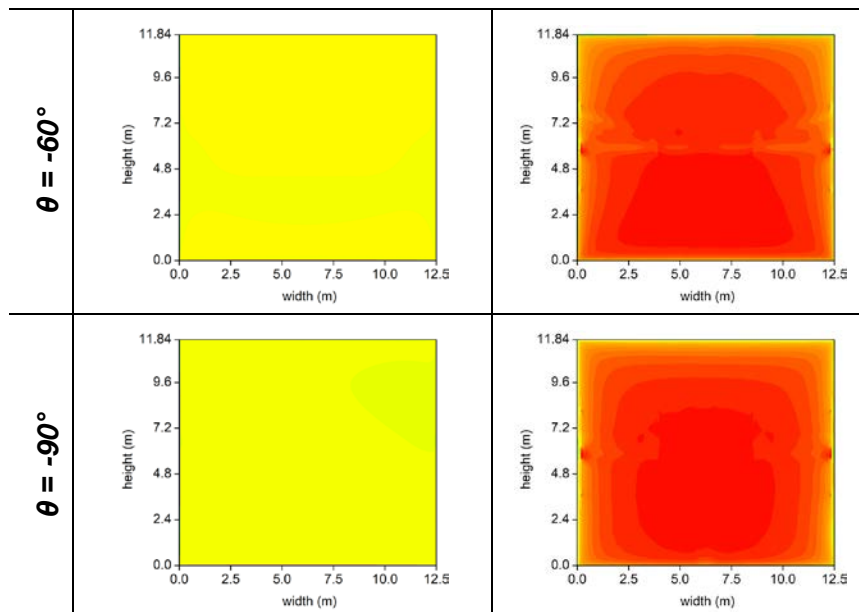


Figure 10. Pressure distribution on the heliostat at wind speed of 20 m/s

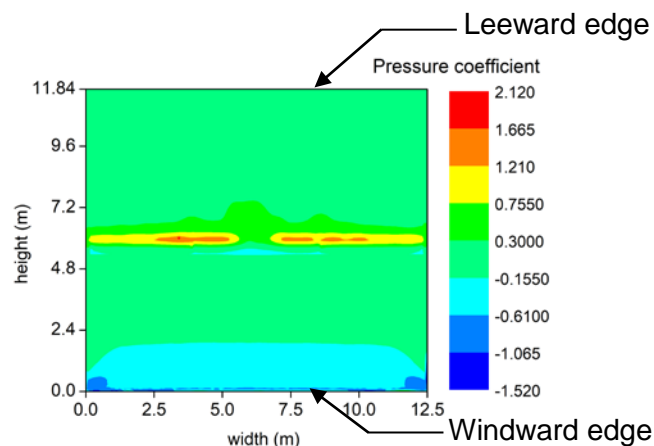
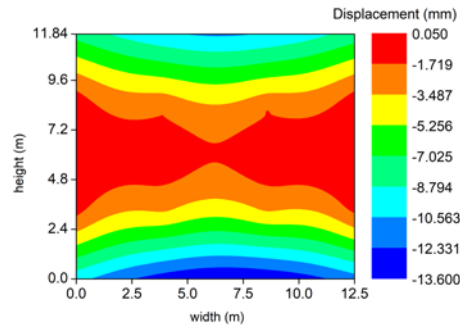


Figure 11. Surface pressure coefficient distribution on the stowed heliostat

Having discussed the distributions of wind pressure on the heliostat surfaces, it was decided to evaluate the structural behaviour characteristics of the heliostat's sandwich composite panel in great detail. Figure 12 presents the displacement distributions of the heliostat surface for the aforementioned tilt angles.

At the tilt angle $\theta = 90^\circ$, the areas with maximum displacement values are located at the heliostat's lower and upper edge regions, with higher displacement values located at the upper edge. As the structure's tilt angle gradually decreases from $\theta = 90^\circ$ to $\theta = 30^\circ$, the structure experiences larger displacement values at the reflector surface's lower edge. This is due to, as addressed previously, the progressive shift in the high-pressure regions at the heliostat's structure towards the lower edge as the tilt angle varies from 90° to 30° .

As the structure's tilt angle changes from $\theta = 30^\circ$ to $\theta = 0^\circ$, the recorded maximum displacement values significantly decrease. This is due to, as discussed previously, the very small area in the front side of the reflector directly facing the wind that allows incoming flow



(g) $\theta = -90^\circ$

Figure 12. Displacement distribution of the heliostat surface at wind speed of 20 m/s for different tilt angles

In all of the cases studied, the largest resultant displacement is of 19.6 mm taking place at tilt angle of 30° . According to Kolb et al. (2007), the Sandia requirements defined the maximum allowable reflective surface displacement angle caused by wind to be 3.6 mRad. Based on the aforementioned requirement, Björkman (2014) presented an approach, demonstrated in Figure 13, to evaluate the performance of the heliostat's reflective surface using the following triangular relationship (Equation (11)) to calculate the maximum allowable displacement:

$$\tan(\pm 3.6 \text{ mRad}) = \frac{\text{Displacement}}{\frac{1}{2}(\text{Heliostat chord length})} \quad (11)$$

Using Equation 11, and given that the heliostat's chord length is 11.84 m, the calculated maximum allowable deflection was found to be approximately ± 21.3 mm. On this basis, the deformation of the structure from the simulation suggests that it is within the allowable threshold, and may be suitable for use as a heliostat.

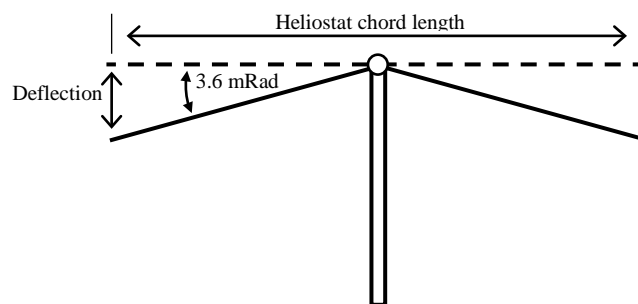


Figure 13. Interpretation of the reflective surface's maximum allowable deflection

Under the same worst case scenario, the highly stressed regions are located at the lower aluminum sheet of the sandwich panel, primarily at its junction with the supporting steel attachments (Figure 14). The calculated maximum von Mises equivalent stress is of 121.62 MPa, which is well below the aluminum's yield strength (280 MPa). This indicates the given heliostat's composite structure, with an achieved weight reduction of approximately 20% compared to an existing 148 m² steel-based heliostat manufactured by Advanced Thermal Systems (ATS) (Kolb et al., 2007), is unlikely to experience material failure and is expected to maintain a very high optical performance when subjected to a wind of 20 m/s and below.

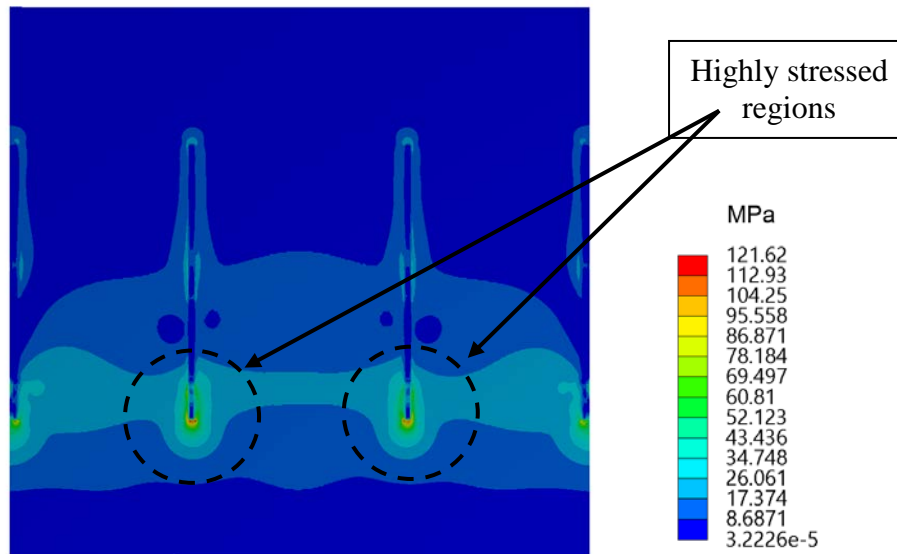


Figure 14. von Mises equivalent stress distributions at the lower aluminum sheet of the sandwich panel

4. Conclusions

The present study was undertaken to investigate the aero-structural robustness and behaviour characteristics of sandwich composites when employed as a heliostat mirror support structure by performing numerical fluid-structure interaction (FSI) simulations. The numerical FSI model's accuracy was verified by comparing the CFD predictions of the heliostat's mean drag and lift coefficients and the FEA modal frequency results with both experimental measurements and numerical results from previously published work. The obtained results showed reasonable agreement, confirming the validity of the FSI model.

From this the study showed that, among all of the operational conditions investigated, the worst case is found to be at a tilt angle of 30°. According to the structural displacement distributions of the heliostat surface for the aforementioned tilt angle, the maximum resultant displacement is of 19.6 mm taking place at the lower edge of the reflector. This will not cause significantly detrimental effect on the reflector's optical performance, according to relevant optical performance standards. Simulations also indicate no structural failure is predicted for the sandwich composite under the same worst case scenario according to the von Mises failure criterion. The overall result of this is that the proposed heliostat's composite structure is unlikely to experience material failure and is expected to maintain a very high optical performance when subjected to a wind of 20 m/s and below.

To deliver a much better understanding on how honeycomb sandwich composites respond under wind effects, future considerations of this work will involve performing the previously conducted analyses for additional wind speeds with various tilt and wind incidence angles. Furthermore, the sensitivity of the mirror displacements to the tensile and compressive loading on the composite panel structure, the structural fatigue of the steel support trusses and the bending and torsional loads on the torque tube needs also to be further investigated.

References

ANSYS Inc. 2015. FLUENT user's guide, ANSYS, Canonsburg.



- Ayub, M.Y., Ahmer, Z., Khan, S.R. and Shah, M.A, 2011, 'Mechanical behavior characterization of aluminum based honey comb structure by optimized modeling and numerical simulations', *Journal of Space Technology*, 1(1), p26-33.
- Björkman, N., 2014, Heliostat design. Master Thesis, Department of Industrial Engineering and Management, KTH Royal Institute of Technology, Stockholm, Sweden.
- Emes, M.J., Ghanadi, F., Arjomandi, M., and Kelso, R.M, 2018, 'Investigation of peak wind loads on tandem heliostats in stow position', *Renewable Energy*, 121, p548-558.
- Gibson, L.J. and Ashby, M.F, 1997, 'Cellular solids: Structure and properties', 2nd Edition, Cambridge University Press, Cambridge.
- Gong, B., Li, Z., Wang, Z. and Wang, Y, 2012, 'Wind-induced dynamic response of Heliostat', *Renewable Energy*, 38(1), p206-213.
- Google, 2011. RE<C: Heliostat wind tunnel experiments. Available from <http://www.google.org/pdfs/google_heliostat_wind_tunnel.pdf>. (accessed 15th August, 2017).
- Heimbs, S., Vogt, D., Hartnack, R., Schlattmann, J. and Maier, M, 2008, 'Numerical simulation of aircraft interior components under crash loads', *International Journal of Crashworthiness*, 13(5), p511-521.
- Hutchins, N., Chauhan, K., Marusic, I., Monty, J. and Klewicki, J, 2012, 'Towards Reconciling the Large-Scale Structure of Turbulent Boundary Layers in the Atmosphere and Laboratory', *Boundary-Layer Meteorology*, 145(2), p273-306
- Jubayer, C.M. and Hangan, H, 2014, 'Numerical simulation of wind effects on a stand-alone ground mounted photovoltaic (PV) system', *Journal of Wind Engineering and Industrial Aerodynamics*, 134, p56-64.
- Kolb, G., Jones, S., Donnelly, M., Gorman, D., Thomas, R., Davenport, R. and Lumia, R, 2007, 'Heliostat cost reduction study', Sandia National Laboratories, Albuquerque, New Mexico, Report number SAND2007-3293.
- Kolb, G.J., Ho, C.H., Mancini, T.R. and Gary, J.A, 2011, 'Power tower technology roadmap and cost reduction plan', Sandia National Laboratories, Albuquerque, New Mexico, Report No. SAND2011-2419.
- Lee, K., Huque, Z., Kommalapati, R. and Han, S.E, 2017, 'Fluid-structure interaction analysis of NREL phase VI wind turbine: Aerodynamic force evaluation and structural analysis using FSI analysis', *Renewable Energy*, 113, p512-531.
- Nast, E, 1997, 'On Honeycomb-Type Core Moduli', *Presented at the Collection of Technical Papers-AIAA/ASME/ASCE/AHS/ ASC Structures, Structural Dynamics and Materials Conference*, 2, p1035-1044.
- Peterka, J.A., Hosoya, N., Bienkiewicz, B. and Cermak, J.E, 1986, 'Wind load reduction for heliostats', Report SERI/STR-253-2859. Solar Energy Research Institute, Golden, Colorado, USA.
- Peterka, J.A. and Derickson, R.G, 1992, 'Wind load design methods for ground-based heliostats and parabolic dish collectors', Report number SAND92-7009. Sandia National Laboratories, Albuquerque, NM (United States).

Schwingshackl, C.W., Aglietti, G.S. and Cunningham, P.R, 2006, 'Determination of honeycomb material properties: Existing theories and an alternative dynamic approach', *Journal of Aerospace Engineering*, 19(3), p177-183.

Simiu, E. and Scanlan, R.H, 1996, 'Wind Effects on Structures: Fundamentals and Applications to Design', Third ed. John Wiley & Sons Wiley, New York

Sorohan, Ş., Constantinescu, D.M., Sandu, M. and Sandu, A.G, 2016, 'Assessment of effective elastic properties of honeycomb cores by modal finite element analyses', *Proceedings of the European Automotive Congress EAEC-ESFA 2015*, p443-454.

Uzair, M., Anderson, T.N. and Nates, R.J, 2017, 'The impact of the parabolic dish concentrator on the wind induced heat loss from its receiver', *Solar Energy*, 151, p95-101.

Uzair, M., Anderson, T.N. and Nates, R.J, 2018, 'Modeling of convective heat loss from a cavity receiver coupled to a dish concentrator', *Solar Energy*, 176, p496-505.

Zenkert, D, 1997, 'The handbook of sandwich construction', EMAS Ltd., West Midlands.

Appendix A

As noted, the computational domain was extended upstream from the heliostat in order to allow the boundary layer to develop. Figure 15 illustrates that both the velocity and turbulence intensity profiles incident on the heliostat compare well with field experimental data collected by Hutchins et al. (2012) in a real atmospheric boundary layer. The obtained velocity and turbulence intensity profiles, demonstrate that the upstream extension of the computational domain was sufficient to allow the boundary layer to develop, with a turbulence intensity (I_u) of 14.6% measured at 10 meters above ground. Furthermore, this value falls within the range of turbulence intensities usually measured near the ground for an open field environment; between 11% for flat desert terrain and 17% for open country with isolated trees and buildings (Peterka and Derickson, 1992; Simiu and Scanlan, 1996).

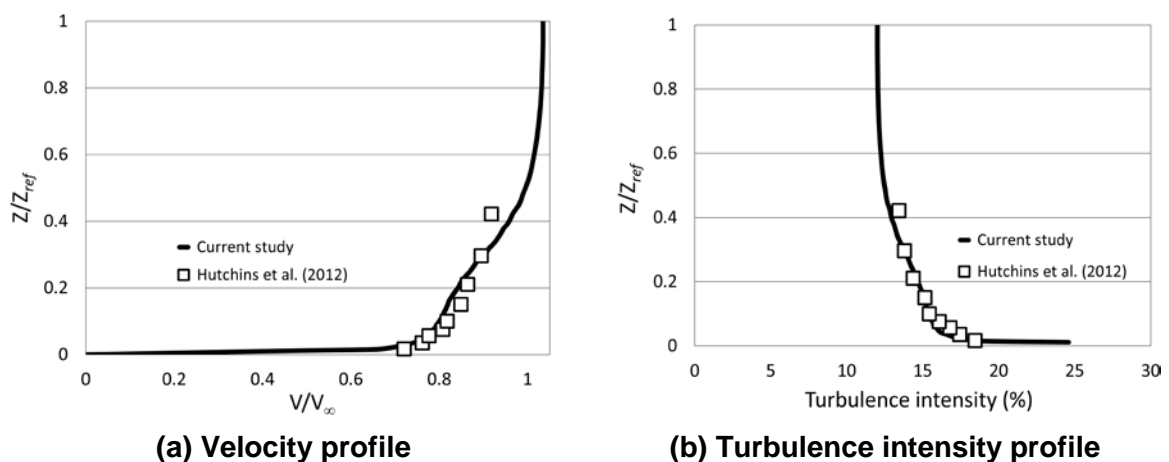


Figure 25. Incident velocity and turbulence intensity profiles

Appendix B

Nomenclature



ASIA-PACIFIC
SOLAR RESEARCH
CONFERENCE

t	Sheet thickness	E₃	Aluminum honeycomb core modulus of elasticity in direction 3
a	Cell wall length	v₁₂	Aluminum honeycomb core Poisson's ratio in plane 1–2
φ	Core angle	v₂₃	Aluminum honeycomb core Poisson's ratio in plane 2–3
E	Modulus of elasticity of Aluminum	v₁₃	Aluminum honeycomb core Poisson's ratio in plane 1–3
v	Poisson's ratio of Aluminum	G₁₂	Aluminum honeycomb core shear modulus in plane 1–2
G	Shear modulus of Aluminum	G₂₃	Aluminum honeycomb core shear modulus in plane 2–3
ρ	Density of Aluminum	G₁₃	Aluminum honeycomb core shear modulus in plane 1–3
E₁	Aluminum honeycomb core modulus of elasticity in direction 1	ρ_{honeycomb}	Density of Aluminum honeycomb core
E₂	Aluminum honeycomb core modulus of elasticity in direction 2		

$$E_1 = \frac{t^3 (1 + \sin \varphi)}{12 \alpha^3 \cos^3 \varphi \left[\frac{\cos \varphi}{8} - \frac{1 + \cos \varphi}{8} \right] (1 - \nu^2)} E \quad (1)$$

$$E_2 = \frac{t^3 \cos \varphi}{(1 + \sin \varphi) \alpha^3 \sin^2 \varphi (1 - \nu^2)} E \quad (2)$$

$$E_3 = \frac{2 t}{\alpha \cos \varphi (1 + \sin \varphi)} E \quad (3)$$

$$G_{12} = \frac{t^3 (1 + \sin \varphi)}{\alpha^3 (1 - \nu^2) \cos \varphi (6.25 - 6 \sin \varphi)} E \quad (4)$$

$$G_{23} = \frac{10 t}{9 \alpha \cos^3 \varphi (1 + \sin \varphi)} G \quad (5)$$

$$G_{13} = \frac{2 t}{\alpha \cos \varphi (1 + \sin \varphi)} G \quad (6)$$

$$\nu_{12} = \frac{\sin^2 \varphi (1 + \sin \varphi)^2}{12 \alpha^3 \cos^3 \varphi \left[\frac{\cos \varphi}{8} - \frac{1 + \cos \varphi}{8} \right]} \quad (7)$$

$$\nu_{23} = \frac{t^2 \cos^2 \varphi}{2 \alpha^2 \sin^2 \varphi (1 - \nu^2)} \nu \quad (8)$$

$$\nu_{13} = \frac{t^2 (1 + \sin \varphi)^2}{24 \alpha^2 \cos \varphi \left[\frac{\cos \varphi}{8} - \frac{1 + \cos \varphi}{8} \right]} * \frac{\nu}{(1 - \nu^2)} \quad (9)$$

$$\rho_{honeycomb} = \frac{3 t}{2 \alpha \cos \varphi (1 + \sin \varphi)} \rho \quad (10)$$